

Two-dimensional mapping of surface scatterers on an optical fiber core using selective mode launching

Cite as: APL Photonics 6, 026105 (2021); <https://doi.org/10.1063/5.0036300>

Submitted: 03 November 2020 . Accepted: 27 January 2021 . Published Online: 12 February 2021

 Lu Peng,  Linh Viet Nguyen,  Jiawen Li,  Nicolas Riesen,  Dale Otten,  David G. Lancaster,  Heike Ebandorff-Heidepriem, and  Stephen C. Warren-Smith



View Online



Export Citation



CrossMark

ARTICLES YOU MAY BE INTERESTED IN

[Fast and sensitive diffuse correlation spectroscopy with highly parallelized single photon detection](#)

APL Photonics 6, 026106 (2021); <https://doi.org/10.1063/5.0031225>

[Distributed Bragg reflectors from colloidal trilayer flake solutions](#)

APL Photonics 6, 026104 (2021); <https://doi.org/10.1063/5.0036052>

[Two-step manufacturing of hundreds of meter-long silicon micrometer-size core optical fibers with less than 0.2 dB/cm background losses](#)

APL Photonics 6, 026101 (2021); <https://doi.org/10.1063/5.0028195>

APL Photonics
Become a member of the
Early Career Advisory Board

[Find out how](#)



Two-dimensional mapping of surface scatterers on an optical fiber core using selective mode launching

Cite as: APL Photon. 6, 026105 (2021); doi: 10.1063/5.0036300

Submitted: 3 November 2020 • Accepted: 27 January 2021 •

Published Online: 12 February 2021



Lu Peng,^{1,2,3,a)}  Linh Viet Nguyen,^{1,2,4}  Jiawen Li,^{2,3,5}  Nicolas Riesen,^{1,2,4}  Dale Otten,⁴ 
David G. Lancaster,⁴  Heike Ebendorff-Heidepriem,^{1,2,3}  and Stephen C. Warren-Smith^{1,2,3,4} 

AFFILIATIONS

¹School of Physical Sciences, The University of Adelaide, Adelaide SA 5005, Australia

²Institute for Photonics and Advanced Sensing, The University of Adelaide, Adelaide SA 5005, Australia

³Australian Research Council Centre of Excellence for Nanoscale Biophotonics, Adelaide SA 5005, Australia

⁴Future Industries Institute, University of South Australia, Mawson Lakes SA 5095, Australia

⁵Adelaide Medical School, The University of Adelaide, Adelaide SA 5005, Australia

^{a)} Author to whom correspondence should be addressed: lu.peng@adelaide.edu.au

ABSTRACT

The tracking of small particles is an important but challenging task for biological applications such as disease diagnostics and medical research. Current methods are limited to the use of bulky instruments such as flow cytometers and microscopes. Here, a novel technique for the detection and measurement of micron-scale optical scatterers using a few-mode exposed-core microstructured optical fiber is proposed. Through selective mode launching combined with optical frequency domain reflectometry, scatterers located on the fiber core surface can be simultaneously mapped with both longitudinal and transverse information. This technique is demonstrated by detecting the two-dimensional positions of several femtosecond-laser-inscribed micron-scale ablations written at different locations on the fiber core surface. Due to the compact nature of the optical fiber and its local sensitivity to scatterers that are in close proximity to it, this technique has the potential for the measurement and detection of micron-scale particles in difficult to reach biological environments for *in vivo* applications.

© 2021 Author(s). All article content, except where otherwise noted, is licensed under a Creative Commons Attribution (CC BY) license (<http://creativecommons.org/licenses/by/4.0/>). <https://doi.org/10.1063/5.0036300>

I. INTRODUCTION

Significant effort has been invested in manipulating and measuring small particles with light in order to enrich our knowledge of the dynamics and interactions of the microscale world.^{1–5} The use of optical fibers for this purpose is gaining interest due to their small size and flexibility, allowing them to reach into difficult-to-access regions, such as deep inside the body. For example, advanced techniques for particle tracking include the use of optical fiber probes with microlenses to trap and manipulate targeted cells⁶ and holographic manipulation of particles via a multimode fiber.⁷ The manipulation of particles can also allow them to be exploited for sensing, exemplified by the demonstration of controlled propagation

of micron-scale particles inside hollow core fibers for high spatial resolution temperature and electric field sensing.^{8,9}

Sensing and tracking small targets is motivated by a desire to understand their presence, size, dynamics, and interactions within microscale and even nanoscale biological environments, with an aim toward disease diagnostics, medical research, and drug delivery.^{4,5,10} Optical fiber based approaches include the detection of nanoparticles using a tapered nanofiber pair,¹¹ the use of an exposed-core microstructured optical fiber (ECF) coupled with a dark-field heterodyne measurement technique,¹² and evanescent field based fluorescence detection of upconversion nanocrystals in microstructured optical fibers.¹³ Fiber-based schemes with the ability to detect spatial information of micro-/nano-objects have also been reported, such as

the use of a nanofluidic fiber for single virus detection,¹⁴ a similar nanofluidic fiber sensor for three-dimensional detection of nano-objects,¹⁵ and a hollow core fiber to study the Brownian motion of nano-objects.¹⁶ Although these methods are able to image nanoscale particles, they rely on bulky external optics that increase the system complexity and prevent their implementation as an *in vivo* device.

Parallel efforts for fiber-based *in vivo* sensing probes have been reported including the integration of simultaneous temperature sensing and optical coherence tomography¹⁷ and pH measurements for surgical assistance.¹⁸ However, these fiber tip-based probes are single-point sensors that must move over a region to collect spatial information, potentially leading to additional mechanical damage of delicate biological tissues. We recently reported a silk-coated *in vivo* ECF-based sensor, which collects information along the entire fiber length but was still limited as an averaged fluorescence measurement without the capability of providing spatial information.¹⁹ There is a need for advancing these techniques to obtain spatial information within confined and challenging biological systems.

To achieve a portable fiber-based device with a long detection range and micron-scale resolution, we seek to apply a technique known as optical frequency domain reflectometry (OFDR),²⁰ which allows for distributed sensing along an optical fiber with high spatial resolution. Our ECF has an exposed channel enabling direct evanescent field contact with the ambient environment without the need for post-processing procedures, enabling repeatable and robust sensing measurements. We recently demonstrated that micron-scale particles could be detected along an ECF using OFDR.²¹ This method could detect the presence and longitudinal position of scattering particles, but not their size or transverse position. In this paper, we propose and experimentally demonstrate a novel approach that adds transverse information to this

method through the selective launching of several modes in a few-mode ECF. Using the numerically simulated evanescent field profiles of the optical modes, we add the ability to detect a scatterer's transverse position using a matrix approach, thus demonstrating two-dimensional (2D) sensing. We anticipate this technique could be deployed for micron-scale particle detection based on a single fiber path for disease diagnostics and drug delivery in clinical applications.

II. CONCEPT

We demonstrate our technique using an in-house fabricated ECF as shown in Fig. 1(a), with the yellow dashed core region magnified in Fig. 1(b). Our ECF has a core diameter of $7.5\ \mu\text{m}$ and a mode field diameter of $5.18\ \mu\text{m}$ for the horizontally polarized fundamental mode (FM) (i.e., polarized parallel to the exposed surface) at a wavelength of $1550\ \text{nm}$. The fabrication of this ECF has been described previously.²² To achieve 2D distributed sensing, the few-mode nature of the ECF plays a key role. As illustrated in Fig. 1(c), scatterers (shown as red dots) located at different transverse positions across the ECF core surface interact with different modes, such as those displayed in Figs. 1(d)–1(f), with different strengths due to their varying spatial distribution of energy across the core surface. For example, Fig. 1(d) shows the Poynting vector distribution of the fundamental mode (FM), which can interact most strongly with a scatterer located at the core center. Compare this to the higher-order modes in Figs. 1(e) and 1(f) labeled HOM_1 and HOM_2 , which can interact relatively more strongly with scatterers at different offset positions away from the center. Figure 1(g) shows the time averaged z-component (propagating component) of the Poynting vector for the three modes considered along the exposed boundary of the ECF [dashed yellow line in Figs. 1(d)–1(f)] and the

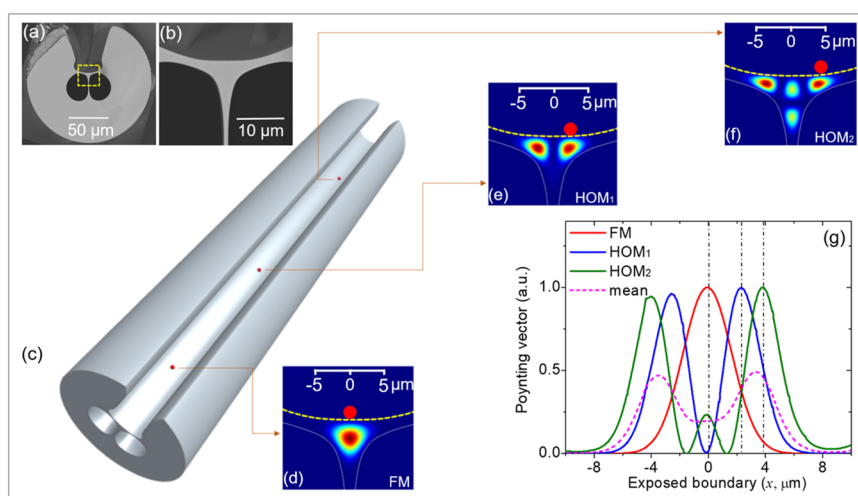


FIG. 1. (a) Scanning electron microscope (SEM) image of the ECF. (b) Core region of the ECF corresponding to the yellow dashed box in (a). (c) Illustration of the ECF with scatterers (red points) located at different longitudinal and transverse positions along the exposed channel. These scatterers can interact with different propagating transverse optical modes as shown in (d)–(f), depending on their transverse offset from the center. (g) Calculated Poynting vector distributions (normalized to 1) of several selected modes on the exposed boundary [yellow dashed line in (d)–(f)], while the magenta dashed curve shows the mean of three modes. Dashed dark lines correspond to scatterers (d)–(f) at different transverse positions. All simulations (d)–(g) are based on the finite element method (COMSOL) using a free space wavelength of $1550\ \text{nm}$.

mean of the three modes (dashed magenta curve) using the following expression:²³

$$P_m(x) = \frac{1}{2} |a_m|^2 \text{Re} \left\{ \hat{e}_m(x) \times \hat{h}_m(x) \cdot \hat{z} \right\}, \quad (1)$$

where a_m is the modal coefficient for the m th mode (FM, HOM₁, and HOM₂), \hat{e}_m and \hat{h}_m are the orthonormal electric and magnetic fields for each mode, respectively, and x represents the distance along the ECF exposed boundary (as opposed to a Cartesian coordinate), with $x = 0$ at the center of the core. In Fig. 1(g), the modal amplitudes have been adjusted such that the plot is normalized to unity to clearly see the variation in energy distribution at the exposed-core surface for the three modes considered. Note that in this work, including the above simulated modes and the following experiments, we consider only the horizontally polarized modes as they generally have greater field intensity at the surface compared to vertically polarized modes. The black dashed lines in Fig. 1(g) indicate scatterers at different transverse positions crossing the ECF boundary corresponding to Figs. 1(d)–1(f), respectively, showing how the different modes interact with scatterers at different transverse positions.

We now describe how multiple launched optical modes can be used to determine quantitative transverse spatial information about the size and position of scatterers. We assume that the returned scattered signal is first longitudinally resolved using OFDR and our task is now to resolve the transverse position using the scatter from multiple modes. We assume that the returned signal intensity from each scatterer is proportional to the evanescent field of the particular excited optical mode and its overlap with the scatterer at the surface. This neglects the evanescently coupled distribution of backscatter into the counter-propagating modes of the fiber but allows us to consider the system using a linear matrix approach. We then spatially divide the transverse location across the core into discrete regions that equal the number of modes. For example, if we launch three optical modes, then the transverse region can be resolved into three separate regions. In the general case of N modes, we can resolve into N regions and write the total scattered light for each mode using the following expression:

$$I_m = u_1 \int_{R_1} P_m(x) dx + u_2 \int_{R_2} P_m(x) dx + \dots + u_N \int_{R_N} P_m(x) dx, \quad (2)$$

where I_m is the returned signal from the OFDR measurement for a given longitudinal position for the m th launched optical mode and u_i is a scattering factor that represents the degree of returned scatter signal from the i th transverse region R_i . This can be expressed as the following matrix equation:

$$\vec{I} = M\vec{u}, \quad (3)$$

where $\mathbf{I} = (I_1, I_2, \dots, I_N)$, $\mathbf{u} = (u_1, u_2, \dots, u_N)$, and M is an $N \times N$ matrix given by

$$M = \begin{bmatrix} \int_{R_1} P_1 & \int_{R_2} P_1 & \dots & \int_{R_N} P_1 \\ \int_{R_1} P_2 & \dots & & \vdots \\ \vdots & & & \\ \int_{R_1} P_N & \dots & & \int_{R_N} P_N \end{bmatrix}. \quad (4)$$

We can then solve for the unknown scatter vector \mathbf{u} through a matrix inversion,

$$\vec{u} = M^{-1}\vec{I}. \quad (5)$$

In order to implement this approach in practice, the matrix M is calculated using the numerically simulated Poynting vector distributions as shown in Fig. 1(g) where the regions can be arbitrarily defined but should approximately match the spatial extent of the launched modes. The vector \mathbf{I} is the experimentally measured values from the OFDR signal. In the following experimental results, we demonstrate the application of this method for the three modes shown in Fig. 1 to yield both longitudinal and transverse spatial locations of surface scatters. We note, however, that the same technique could be applied to any number of supported optical modes, provided they can be discretely launched, and for any location of scatterers including inside the waveguide and not only on the surface.

III. RESULTS AND DISCUSSION

A. Inscription of surface scatterers and experimental setup

Scatterers were introduced to the ECF surface using a femtosecond (fs) laser writing technique, which produces permanent silica-air ablation points. A wavelength doubled (524 nm), ultra-fast laser (IMRA DE0210) was used with pulse duration <250 fs and pulse energy of 150 nJ. The ECF was imaged using the same lens as used for the fs laser writing to locate the optical fiber core, similar to a method previously used for fiber Bragg grating inscription.²⁴ Seven points were written in total, as indicated by the red spots with numbers from 1 to 7 in Fig. 2(a), which have a longitudinal spacing of 500 μm between each point and a transverse spacing of 1 μm. The ablation point number 4 was written with a transverse position as close to the center of the optical fiber core as possible, within experimental error. The ECF sample viewed under a camera with visible (red) laser light coupled into the core to show the scatterer locations is shown in Fig. 2(b). The left-hand side red dot in Fig. 2(b) corresponds to the input end of the ECF, while the furthest right-hand side red dot in the dashed yellow box is the seventh ablation point.

The OFDR signal was generated by a swept wavelength (1510 nm–1590 nm) optical sensor interrogator (National Instruments PXIe-4844), which integrates a source (60 μW) and photodetector with a dynamic range of 40 dB and the sampling rate of 10 Hz. The OFDR signal was then generated by optical interference between the reflection from the cleaved end-face of the ECF due to the air-silica interface [black arrow in Fig. 2(a)] and the reflected light from each introduced fs-laser ablation scattering point (red arrows). The interference from each point can then be demultiplexed by applying a fast Fourier transform (FFT) to convert the interference spectrum into longitudinal spatial information with a resolution of ~10 μm as described previously.²¹

The mode launching was controlled by manually adjusting a three-axis optical stage to adjust the axial and transverse positions. The launched mode(s) was monitored using an infrared camera, and the stage was adjusted until one of the three desired modes supported by the ECF was predominantly launched.

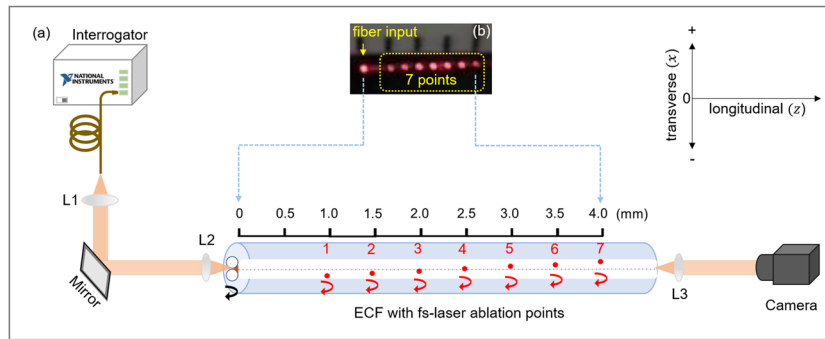


FIG. 2. (a) Schematic of the experimental setup. The black arrow represents reflection at a cleaved surface where $\sim 3.3\%$ of the incident light is reflected back due to the air–silica interface, which is used as the reference to generate the interferometric signal. L1, L2, and L3 are optical lenses. The red points represent fs laser ablation points (numbered from 1 to 7) on the surface of the ECF, and the red arrows depict their scattered signals captured back into the ECF’s guided modes to generate interference with the reference signal. The black scale bar above the ECF shows the axial distributions of the introduced points, with each point separated by $500\ \mu\text{m}$ in the axial direction. The coordinate system is illustrated, where the transverse direction, x , is shown with positive and negative signs from the center of the ECF. The mode launching was monitored at the far end of the ECF using an InGaAs camera. The fiber sample was $\sim 200\ \text{mm}$ in length, and both ends were fixed on three-axis optical stages during the experiments. (b) Image of the fs-laser inscribed fiber sample showing the scattering of red laser light coupled to the ECF core. The ruler image has a $1\ \text{mm}$ scale.

B. OFDR results

Figures 3(a1)–3(c1) show the near field images of the three separately launched modes, which correspond well with the three simulated modes shown in Figs. 3(a2)–3(c2). OFDR traces were then acquired separately for each launched mode, by applying an FFT to the reflected interference spectra. The signal from the seven ablation points can clearly be seen as seven peaks in Figs. 3(a3)–3(c3). Each

peak represents the interference generated between reflection from an ablation point and the cleaved end-face of the ECF, and their longitudinal positions distributed along the ECF are shown on the lower x -axis. As expected from Fig. 2, there is $0.5\ \text{mm}$ spacing between each ablation point, and the points lie within $1\ \text{mm}$ – $4\ \text{mm}$ of the input cleaved end-face of the ECF. We note that there is a small peak at the lower x -axis position of $0.5\ \text{mm}$ in all measured FFT

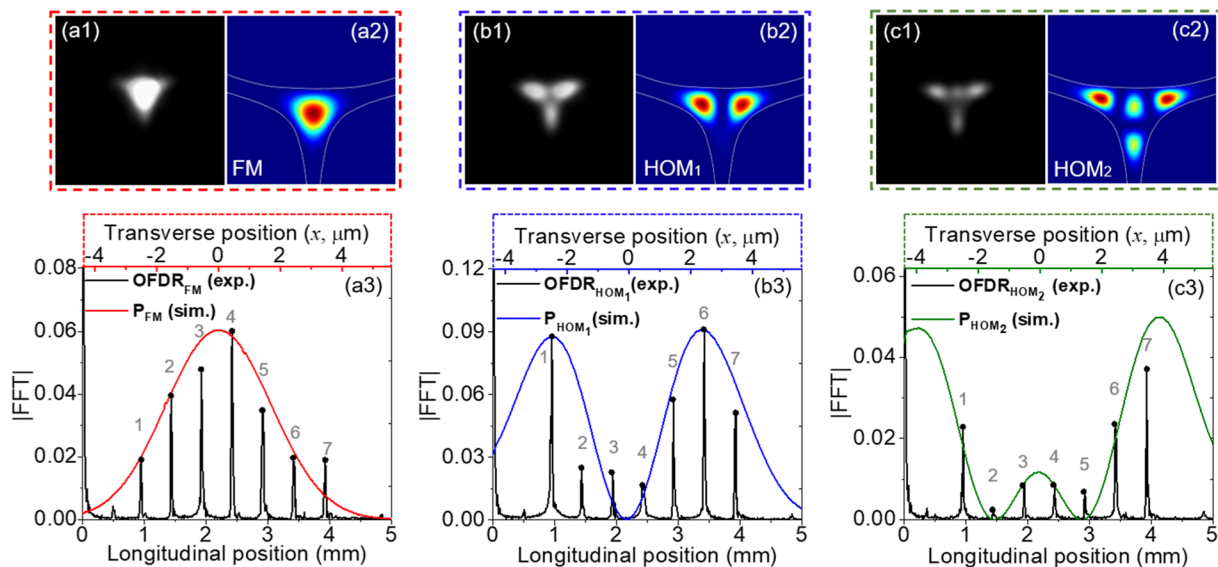


FIG. 3. Experimental measurements under different launch conditions to demonstrate the 2D sensing concept. Real-time near-field mode images are displayed in (a1)–(c1) with their corresponding simulated mode profiles, named as “FM,” “HOM₁,” and “HOM₂,” shown in (a2)–(c2), respectively. (a3)–(c3) The absolute FFT signals (black) are shown with labels “OFDR_{FM} (exp.),” “OFDR_{HOM1} (exp.),” and “OFDR_{HOM2} (exp.);” the bottom axis displays the longitudinal/axial positions of the ablation points (peaks named with numbers “1–7”) on the ECF [see Fig. 2(a)]. The colored curves show the simulated Poynting vector distributions at the ECF surface [red, blue, and green in (a3)–(c3), respectively], which were scaled to best match the height of the FFT peaks (marked as black dots). The top colored axis (secondary x -axis) displays the transverse positions of the ablation points based on the matching process detailed in Sec. III B.

results in Fig. 3. This peak is potentially from the optical interference associated with the regularly longitudinal-spaced ablation points. However, this peak is relatively small compared to the dominant signals, which demonstrates that the scattered light recoupled to the fiber modes is relatively weak compared to the reference signal (from the fiber input end). This is as would be expected for evanescent field recoupling, such as <1% previously calculated for fluorescence-based recoupling.^{25,26} Therefore, undesired multiple scattering from adjacent ablation points is negligible in our demonstration.

Next, we demonstrate visually the validity of our assumption that the returned OFDR signal correlates proportionately with the mode's evanescent field at the surface. We use our prior knowledge of the uniform spacing between the ablation points (1.0 μm spacing) to correlate the OFDR signals with the transverse distance across the ECF surface. This allows us to add the upper x-axis scale in Figs. 3(a3)–3(c3), noting that this is only valid for the OFDR peaks relating to the ablation points as their positions are known and do not apply to, say, other unintended environmental particles (i.e., dust) along the optical fiber. We are then able to overlay the Poynting vector at the ECF surface as shown by the colored curves in Figs. 3(a3)–3(c3) for the three modes, respectively.

The transverse offset of the OFDR data relative to Poynting vector center $x = 0$ (ECF core center) has been adjusted to account for systematic error associated with the positioning of the ablation points across the core, while the height of the simulated Poynting vector curves has been adjusted to best match the FFT peaks to account for errors in the coupling efficiency for the three modes. This was performed by minimizing the following expression:

$$\Delta P_m(x') = \frac{1}{7} \sum_{k=1}^7 |a_m P_{mk}(x) - I_{mk}(x - x')|, \quad (6)$$

where P_{mk} and I_{mk} are the simulated Poynting vector and measured OFDR peak for the m th mode and k th peak, respectively, x' is the transverse offset between the laser writing points and the simulated Poynting vector distributions across the ECF core, k is the scatterer number (1 to 7), and a_m is the vertical scaling of the simulation relative to the OFDR signal.

The transverse offset comes from positioning error in the fs-laser ablation process. While there is a high degree of precision in the relative transverse positions of the ablation points, we expect a systematic error common to all seven points due to the difficulty in visually locating the center of the optical fiber core. By applying Eq. (6) for an arbitrary offset x' , as shown in Fig. 4, we can find the minima position and correct the actual laser writing locations relative to the core center. Figure 4 shows that the simulation and experiment match most closely for a value of $x' = 0.4 \mu\text{m}$, which is within expectations, giving the optical resolution of the imaging system used for identifying the core center during the fs laser writing.

To match the vertical scaling of the Poynting vector simulations for each mode, a_m , with the OFDR peaks, Eq. (6) was again minimized. We first applied the previously determined offset value of $x' = 0.4 \mu\text{m}$ and then evaluated the deviation of each simulated mode with the measured results as a function of a_m (see Fig. S1 in the supplementary material). The minima locations were then determined for each mode, yielding the simulation curves shown in Fig. 3.

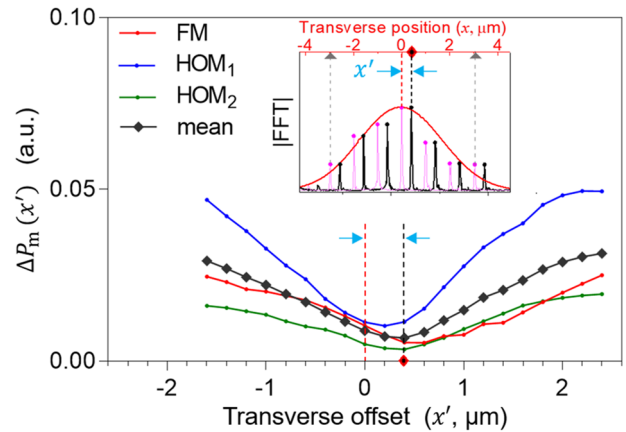


FIG. 4. Determining the transverse offset between the simulated Poynting vector distribution and the OFDR signal averaged for the seven fs-laser ablation points for the three individually launched modes as described by Eq. (6). The mean across the three modes is shown by the black curve, which yields an offset of $x' = 0.4 \mu\text{m}$ as shown by the dashed lines. Inset shows the corresponding shift in the OFDR trace for the fundamental mode.

Note that, in the future, the vertical scaling could equally be achieved through intentional reference points along the ECF, similar to what has been done here, or by accounting for the total coupled power for each mode such as by measuring the ECF output with an optical power meter.

We can see from Fig. 3 that the distribution of the OFDR peaks matches closely with the Poynting vector distributions on the surface, indicating that the linear matrix approach outlined in Sec. II can, indeed, be applied to determine the transverse information about the surface scatterers.

C. Determining scatterer location

We now apply the matrix method in Eq. (5) to determine the transverse location of the scatterers without using the prior knowledge of their location from the laser writing process. Due to the symmetric shape of the Poynting vector distributions shown in Fig. 1(g), we split the transverse regions of the ECF exposed surface by three absolute distances from the center of the core. That is, the integration regions in Eq. (4) are grouped into (i) $0 \mu\text{m} - 1 \mu\text{m}$, (ii) $1 \mu\text{m} - 2 \mu\text{m}$, and (iii) $>2 \mu\text{m}$ from the core center. Integrating the three simulated modes with corrected vertically scaling as discussed in Sec. III B over the three regions yields the following 3×3 (3 modes \times 3 regions) transfer matrix:

$$M = \begin{bmatrix} 0.112 & 0.079 & 0.039 \\ 0.026 & 0.120 & 0.161 \\ 0.016 & 0.003 & 0.038 \end{bmatrix}. \quad (7)$$

Solving Eq. (5) using the matrix in Eq. (7) and the OFDR data (I) yields the results shown in Fig. 5.

The red pixels in Fig. 5(a) show the known locations of the seven fs laser inscribed scatterers according to the positions chosen during the fs laser inscription process, which correspond to the locations presented in Figs. 3(a3)–3(c3). The calculated results in Fig. 5(b) show a strong correlation with the known locations, where

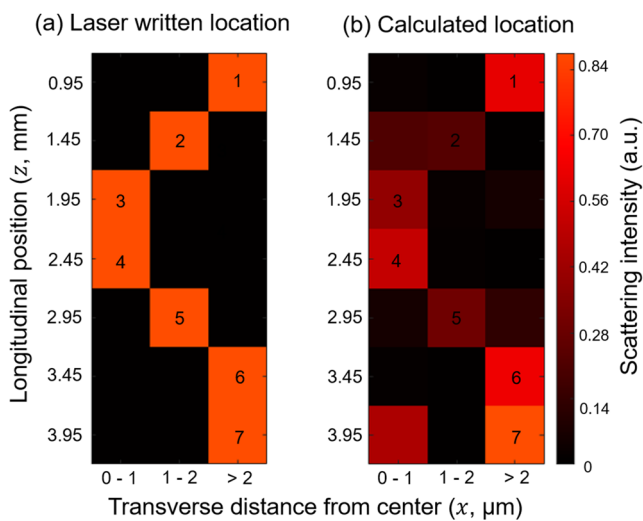


FIG. 5. (a) Fs-laser writing locations grouped into three transverse regions from the center of the ECF core. The numbers 1 to 7 indicate the laser ablation points corresponding to their intended location, factoring the $x' = 0.4 \mu\text{m}$ offset as determined through the results in Fig. 4(b). Measured location of the scatterers using the proposed matrix approach. The y-axis shows the longitudinal position of the scatterers as determined from the OFDR trace.

the pixel with the lightest color in each row represents the most probable area associated with a specific scatterer.

The results in Fig. 5(b) show a strong correlation with Fig. 5(a) but with some variation in intensity and some signal in locations that should show no scattering. We believe the major causes of these discrepancies are as follows. First, the exposed surface is not as flat as other regular quadrate structures, leading to minor inconsistencies in the focus depth for each ablation point when they were written at different locations across the core. This fabrication error may cause differences both in ablation depth and size. A deeper focus, in principle, leads to stronger interaction with the optical field and thus causes greater scatter relative to other surface-only defects. It is also likely that the modes were not launched with 100% efficiency, that is, a small fraction of other modes may have been coupled, which would impact the results particularly where the expected field energy is low. For example, the excitation of the mode HOM_1 in Fig. 3(b1) shows a faint third lobe when only two are expected from the numerical simulation. This could be solved in the future by using advanced coupling techniques such as the use of a spatial light modulator for mode launching,^{27,28} femtosecond-laser-written mode couplers,²⁹ and photonic lanterns.³⁰

D. Discussion

We have demonstrated 2D mapping of single point-like scatterers in the form of surface ablation points. In this work, the fs-laser ablation points are strong scatterers due to the glass-air interface and their position embedded into the core surface and thus would be more strongly scattering than particles located on the core surface. For comparison, we have previously shown that the same configuration can detect much larger scatterers through the evanescent

field, where we detected $10 \mu\text{m}$ polystyrene beads on the fiber surface.²¹ The simulated optical field (see Fig. S2 in the [supplementary material](#)) indicates that the Poynting vector distribution of the fundamental mode (FM) on the exposed surface is 20% of that at a depth beneath the surface of 300 nm (300 nm is an estimation of the average ablation depth beneath the surface²⁴). Therefore, we expect this same technique would be also applicable to surface scatterers through an evanescent field interaction with a trade-off in sensitivity. This could be improved by using an optical detection system of greater dynamic range compared to the 40 dB used in our demonstration. On the other hand, large particles would backscatter with stronger signals and interact more strongly with modes of greater transverse spatial extent. Large particles would thus show signals for more pixels after the matrix method is applied, in addition to a greater extent in the axial OFDR trace.

For this to be effective, the transverse spatial resolution should be improved beyond the currently demonstrated three regions. To improve the transverse resolution, more modes must be launched, which again could be solved using a spatial light modulator, and it would further improve the accuracy of the transfer matrix with more subdivided integration regions with less variation of energy across each region. It is important to note, though, that it is essential that the mode launching is performed, with only individual modes excited, to avoid deleterious inter-modal interference effects. It is also important to avoid mode coupling along the optical fiber length. The ECF used in our work is a high numerical aperture and birefringent fiber (see Table S1 in the [supplementary material](#)), which allows the selected launched modes, including the polarization, to be maintained even under moderate bending (see bending results in Figs. S3 and S4 in the [supplementary material](#)). Mode coupling is dependent on the specific fiber properties and thus needs to be considered before applying our proposed technique.

Another important factor that should be considered is that the three modes launched in this work display highly symmetric properties across the ECF core surface. This is to be expected for an optical fiber with a reflection plane of symmetry, where the Poynting vector distribution follows this symmetry. To obtain information on transverse scatterers where more than one region is involved and obtain an unambiguous result (discriminate positive/negative transverse location), it would be necessary to utilize modes with asymmetric Poynting vector distributions. Due to slight imperfections in the fiber fabrication, the ECF used in our work shows a subtle asymmetry, which leads to asymmetric higher-order modes (see Fig. S5 in the [supplementary material](#)) that could be exploited for this purpose. This would, again, require the use of more complex mode launching techniques or by fabricating an intentionally asymmetric fiber structure to break the symmetry of the supported modes.

IV. CONCLUSION

We have demonstrated a technique for detecting the longitudinal and transverse location of micron-scaled scatterers along an optical fiber using a combination of optical frequency domain reflectometry and selective excitation of transverse guided modes. We have demonstrated this technique using femtosecond laser inscribed ablation points as model scatterers and then comparing the optical response to numerically simulated optical mode profiles. A matrix

approach has been proposed to determine the locations of the surface scatterers, which matches well with the known locations of the laser written ablation points. Although only demonstrated here for mapping the transverse location of single ablation points, our technique can be expanded in the future for the detection of particle size. All the measurements are based on a single fiber path without relying on an external complex side-imaging instrument. We believe the proposed technique has potential for the detection and sizing of biological particles of interest for *in vivo* biomedical applications such as cancer or bacteria detection or the tracking of drug delivery particles. Our proposed scheme is not limited to the use of exposed-core fibers or even evanescent field devices, but can be used to detect the location of any scatterer within a waveguide if the waveguide's modes can be individually launched and simulated numerically. The technique could therefore also be applied to the characterization of defects in waveguides or even for the study of the fundamental physics of micro-/nano-particles and their interactions with surfaces or other particles.

SUPPLEMENTARY MATERIAL

See the [supplementary material](#) for additional information mentioned in the main text.

ACKNOWLEDGMENTS

This work was supported by the Ramsay Fellowship provided by the University of Adelaide. The authors would like to thank OptoFab Node of the Australian National Fabrication Facility utilizing Commonwealth and South Australian State Government Funding, China Scholarship Council (Grant No. 201706750012), the Australian Research Council Centre for Nanoscale BioPhotonics (Grant No. CE14010003), the National Heart Foundation (Fellowship Grant No. 102093) and Australian Research Council (ARC) Future Fellowship (FT200100154). The authors acknowledge Evan Johnson and Alastair Dowler for their contribution to fiber fabrication.

DATA AVAILABILITY

The data that support the findings of this study are available from the corresponding author upon reasonable request.

REFERENCES

- 1 A. Ashkin, *Proc. Natl. Acad. Sci. U. S. A.* **94**(10), 4853–4860 (1997).
- 2 A. S. Urban, A. A. Lutich, F. D. Stefani, and J. Feldmann, *Nano Lett.* **10**(12), 4794–4798 (2010).
- 3 J. Li, E. H. Hill, L. Lin, and Y. Zheng, *ACS Nano* **13**(4), 3783–3795 (2019).
- 4 H. Shen, L. J. Tauzin, R. Baiyasi, W. Wang, N. Moringo, B. Shuang, and C. F. Landes, *Chem. Rev.* **117**(11), 7331–7376 (2017).
- 5 M. Liebel, J. T. Hugall, and N. F. van Hulst, *Nano Lett.* **17**(2), 1277–1281 (2017).
- 6 Y. Li, H. Xin, X. Liu, Y. Zhang, H. Lei, and B. Li, *ACS Nano* **10**(6), 5800–5808 (2016).
- 7 I. T. Leite, S. Turtaev, X. Jiang, M. Šiler, A. Cuschieri, P. S. J. Russell, and T. Čizmar, *Nat. Photonics* **12**(1), 33–39 (2018).
- 8 D. S. Bykov, O. A. Schmidt, T. G. Euser, and P. S. J. Russell, *Nat. Photonics* **9**(7), 461–465 (2015).
- 9 D. S. Bykov, S. Xie, R. Zeltner, A. Machnev, G. K. Wong, T. G. Euser, and P. S. J. Russell, *Light: Sci. Appl.* **7**(1), 22 (2018).
- 10 I.-B. Lee, H.-M. Moon, J.-H. Joo, K.-H. Kim, S.-C. Hong, and M. Cho, *ACS Photonics* **5**(3), 797–804 (2017).
- 11 X.-C. Yu, B.-B. Li, P. Wang, L. Tong, X.-F. Jiang, Y. Li, Q. Gong, and Y.-F. Xiao, *Adv. Mater.* **26**(44), 7462–7467 (2014).
- 12 N. P. Mauranyapin, L. S. Madsen, L. Booth, L. Peng, S. C. Warren-Smith, E. P. Schartner, H. Ebdorff-Heidepriem, and W. P. Bowen, *Opt. Express* **27**(13), 18601–18611 (2019).
- 13 J. Zhao, D. Jin, E. P. Schartner, Y. Lu, Y. Liu, A. V. Zvyagin, L. Zhang, J. M. Dawes, P. Xi, J. A. Piper, E. M. Goldys, and T. M. Monro, *Nat. Nanotechnol.* **8**(10), 729–734 (2013).
- 14 S. Faez, Y. Lahini, S. Weidlich, R. F. Garmann, K. Wondraczek, M. Zeisberger, M. A. Schmidt, M. Orrit, and V. N. Manoharan, *ACS Nano* **9**(12), 12349–12357 (2015).
- 15 S. Jiang, J. Zhao, R. Förster, S. Weidlich, M. Plidschun, J. Kobelke, R. Fatobene Ando, and M. A. Schmidt, *Nanoscale* **12**(5), 3146–3156 (2020).
- 16 R. Förster, S. Weidlich, M. Nissen, T. Wieduwilt, J. Kobelke, A. M. Goldfain, T. K. Chiang, R. F. Garmann, V. N. Manoharan, and Y. Lahini, *ACS Sens.* **5**(3), 879–886 (2020).
- 17 J. Li, E. Schartner, S. Musolino, B. C. Quirk, R. W. Kirk, H. Ebdorff-Heidepriem, and R. A. McLaughlin, *Opt. Lett.* **43**(8), 1682–1685 (2018).
- 18 E. P. Schartner, M. R. Henderson, M. Purdey, D. Dhatrak, T. M. Monro, P. G. Gill, and D. F. Callen, *Cancer Res.* **76**(23), 6795–6801 (2016).
- 19 A. Khalid, L. Peng, A. Arman, S. C. Warren-Smith, E. P. Schartner, G. M. Sylvia, M. R. Hutchinson, H. Ebdorff-Heidepriem, R. A. McLaughlin, B. C. Gibson, and J. Li, *Sens. Actuators, B* **311**, 127864 (2020).
- 20 W. Eickhoff and R. Ulrich, *Appl. Phys. Lett.* **39**(9), 693–695 (1981).
- 21 L. Peng, J. Li, R. A. McLaughlin, H. Ebdorff-Heidepriem, and S. C. Warren-Smith, *Sens. Actuators, A* **303**, 111762 (2020).
- 22 S. C. Warren-Smith and T. M. Monro, *Opt. Express* **22**(2), 1480–1489 (2014).
- 23 A. W. Snyder and J. Love, *Optical Waveguide Theory* (Springer Science & Business Media, 2012).
- 24 S. C. Warren-Smith, R. Kosteki, L. V. Nguyen, and T. M. Monro, *Opt. Express* **22**(24), 29493–29504 (2014).
- 25 V. S. Afshar, Y. Ruan, S. C. Warren-Smith, and T. M. Monro, *Opt. Lett.* **33**(13), 1473–1475 (2008).
- 26 V. S. Afshar, S. C. Warren-Smith, and T. M. Monro, *Opt. Express* **15**(26), 17891–17901 (2007).
- 27 T. G. Euser, G. Whyte, M. Scharer, J. S. Y. Chen, A. Abdolvand, J. Nold, C. F. Kaminski, and P. S. J. Russell, *Opt. Express* **16**(22), 17972–17981 (2008).
- 28 A. Ruskuc, P. Koehler, M. A. Weber, A. Andres-Arroyo, M. H. Frosz, P. S. J. Russell, and T. G. Euser, *Opt. Express* **26**(23), 30245–30254 (2018).
- 29 S. Gross, N. Riesen, J. D. Love, and M. J. Withford, *Laser Photonics Rev.* **8**(5), L81–L85 (2014).
- 30 D. Yu, S. Fu, Z. Cao, M. Tang, L. Deng, D. Liu, I. Giles, T. Koonen, and C. Okonkwo, *Opt. Express* **24**(11), 12192–12201 (2016).